Landslides caused by the March 2019 West Coast storm, South Island, New Zealand

M Wride

SJ de Vilder

GNS Science Report 2020/36
August 2021

GNS SCIENCE
TE PŪ AO

DISCLAIMER

BIBLIOGRAPHIC REFERENCE

Wride M, de Vilder SJ. 2021. Landslides caused by the March 2019 West Coast storm, South Island, New Zealand. Lower Hutt (NZ): GNS Science. 33 p. (GNS Science report; 2020/36). doi:10.21420/H0ZK-ES93.

M Wride, GNS Science, PO Box 30368, Lower Hutt 5040, New Zealand

SJ de Vilder, GNS Science, PO Box 30368, Lower Hutt 5040, New Zealand

www.gns.cri.nz

ISSN 2350-3424 (online)
ISBN 978-1-99-001059-0 (online)
http://dx.doi.org/10.21420/H0ZK-ES93

CONTENTS

FIGURES

TABLES

ABSTRACT

During the week of 25–31 March 2019, the West Coast of the South Island experienced an intense rainstorm. The rain was widespread, extending from Haast to Hokitika, with the highest intensity of rainfall recorded in the range front south of Hokitika. The March 2019 storm resulted in a record amount of rainfall recorded over a 48-hour period in the Cropp River Catchment. The result of this extreme rainfall event was widespread flooding and landslides, including the washout and destruction of the Waiho Bridge on State Highway 6. An aerial reconnaissance was flown by GNS Science on 17 and 18 April 2019, as part of GeoNet landslide response, to identify landslides triggered by the storm. High-resolution SkySat satellite imagery was acquired for a c. 10,000 km² area covering the area of most intense total rainfall, which extended from inland of Hokitika south to Harihari. This satellite imagery, combined with pre-storm event aerial imagery obtained from Land Information New Zealand and Google Earth, was used to map the distribution of landslides that were triggered by the storm. The storm event triggered 1290 landslides within the study area, with the highest spatial densities observed in the hill country surrounding Mount O'Connor, southeast of Hokitika.

The landslide distribution was compared against key physiographic attributes such as rainfall, geology, slope angle, slope aspect and vegetation type to assess controlling influence(s) on landslide failure. The results of our analysis show that the areas of more intense rainfall do not correlate with a greater density of landslides. This disparity could be the result of the interpolated rainfall data not being representative of the true rainfall during the event and may indicate that rainfall was higher than calculated by the linear interpolation of the rain gauge data on slopes nearer to the coast (where there is a higher density of landslides) than those further inland. Additionally, this disparity may be due to variations in rainfall intensity during this 48-hour period, which are not captured in the 48-hour rainfall totals from rain gauge data. Additionally, the limitations of the satellite imagery, which include snow cover and shadow, may have prevented the identification of landslides at higher altitudes. While the density distribution of landslides in the study area does not correlate with rainfall intensity, it does correlate with slope angle and aspect. Landslide density increases with steeper slopes, and north-, northwest- and northeast-facing slopes all display a higher landslide density, which may be related to the characteristics of the rainfall in the storm event. For the major land-cover types, sub-alpine shrub displays the highest landslide density, with 2.96 landslides per km², and accounts for 16.5% of the study area. The dominant land-cover type of indigenous forest, accounting for 51.3% of the study area, only displays a landslide density of 1.64 km².

KEYWORDS

West Coast, South Island New Zealand, March 2019 storm, rainfall-induced landsliding, satellite imagery

This page left intentionally blank.

1.0 INTRODUCTION

1.1 Background

During the week of 25–31 March 2019, the West Coast, South Island, New Zealand, experienced a storm event that resulted in a record amount of rainfall. NIWA reported that the Cropp River waterfall recorded 1086 mm of rainfall over a 48-hour period, which is the highest recorded 48-hour rainfall in New Zealand and exceeds the annual rainfall of some main centres in New Zealand (NIWA Weather 2019).

West Coast Civil Defence declared a state of emergency due to the damage from the storm. This damage included the destruction of the Waiho River bridge near the town of Franz Josef and damage to several roads in the region. The extreme rainfall also caused numerous landslides, with a section of State Highway 6 from Hokitika to Makarora closed because of the hazard posed. The following media stories outline, and contain photographs and videos of, the storm damage:

- https://www.newshub.co.nz/home/new-zealand/2019/03/weather-exceptional-rain-event-on-west-coast-expected-to-worsen.html
- http://floodlist.com/australia/new-zealand-floods-western-region-march-2019

A GeoNet landslide response was undertaken after the storm to record the nature, extent and impact of landsliding across the West Coast region. This report provides the findings of the March 2019 West Coast storm GeoNet response and specifically aims to identify the size, number, distribution and impacts of landslides that occurred across the region and their relationship to key physiographic characteristics, including rainfall, geology, land cover, slope angle, slope aspect and elevation.

1.2 Rainfall Characteristics

Between 25 and 27 March 2019, the West Coast experienced a south-westerly storm that brought intense rainfall and broke national records for the amount of rain recorded over a 48 hour period. Rainfall data were obtained from the National Climate Database (https://cliflo.niwa.co.nz/) and West Coast Regional Council rain gauges in the South Island for the 48-hour period of rainfall between 25 and 27 March. The data were interpolated using the Natural Neighbour tool in ArcGIS to approximate the rainfall between the rain gauges and to create a map of rainfall for the area that was most affected by the storm (Figure 1.1). As Figure 1.1 shows, the highest rainfall was recorded in the range front immediately to the southeast of Hokitika, including the Cropp River catchment where the record national 48-hour rainfall total was recorded. However, heavy rain was recorded all along the West Coast from Haast to Hokitika and in Fiordland. MetService defines heavy rain as rainfall in an area of 1000 km^2 or more of >50 mm over 6 hours or >100 mm over 24 hours (MetService 2008–2021).

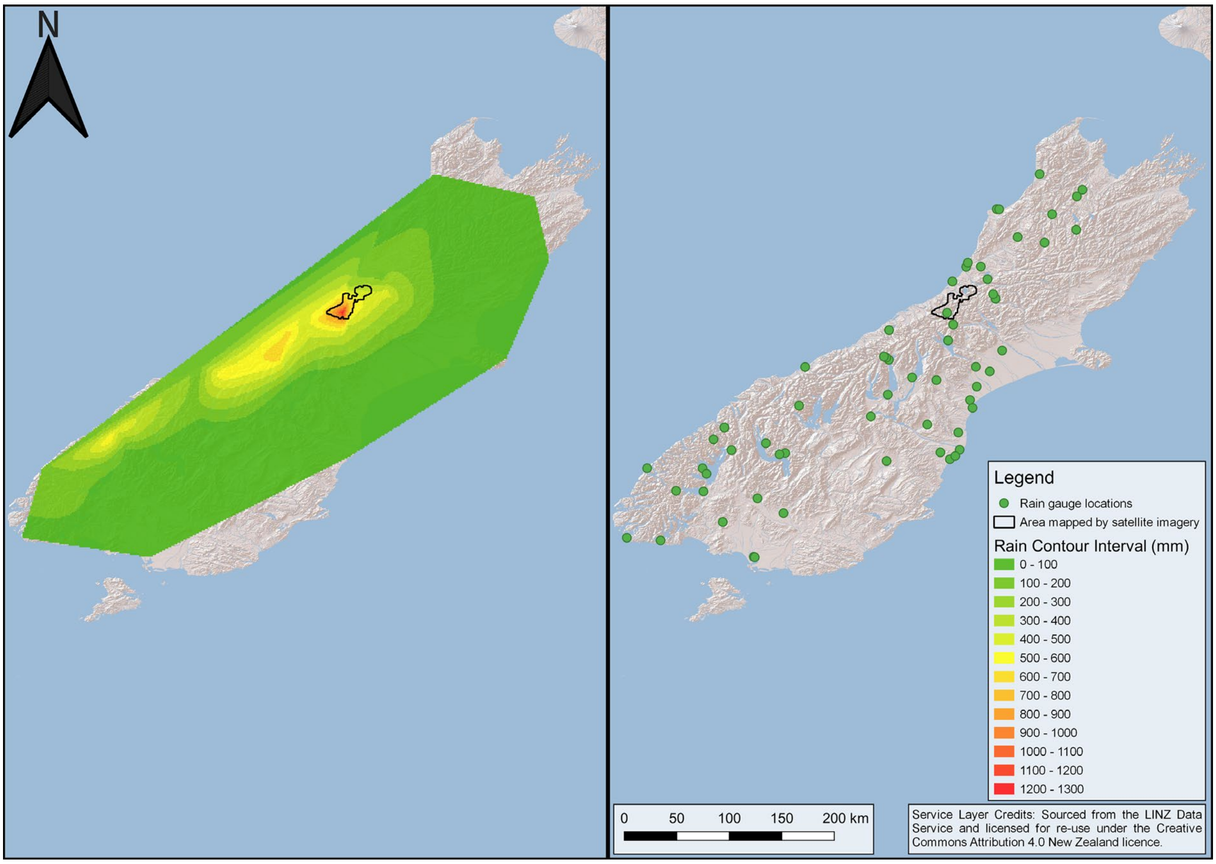

Figure 1.1 South Island rain gauges and rainfall contour for March 2019 event.

1.3 Aerial Reconnaissance Flight

An aerial reconnaissance was flown by helicopter on Wednesday 17 and Thursday 18 April by Saskia de Vilder and Dougal Townsend (GNS Science). The flight path focused on areas where landslides had been reported, as well as on determining the extent of landsliding due to the widespread heavy rainfall (Figure 1.2).

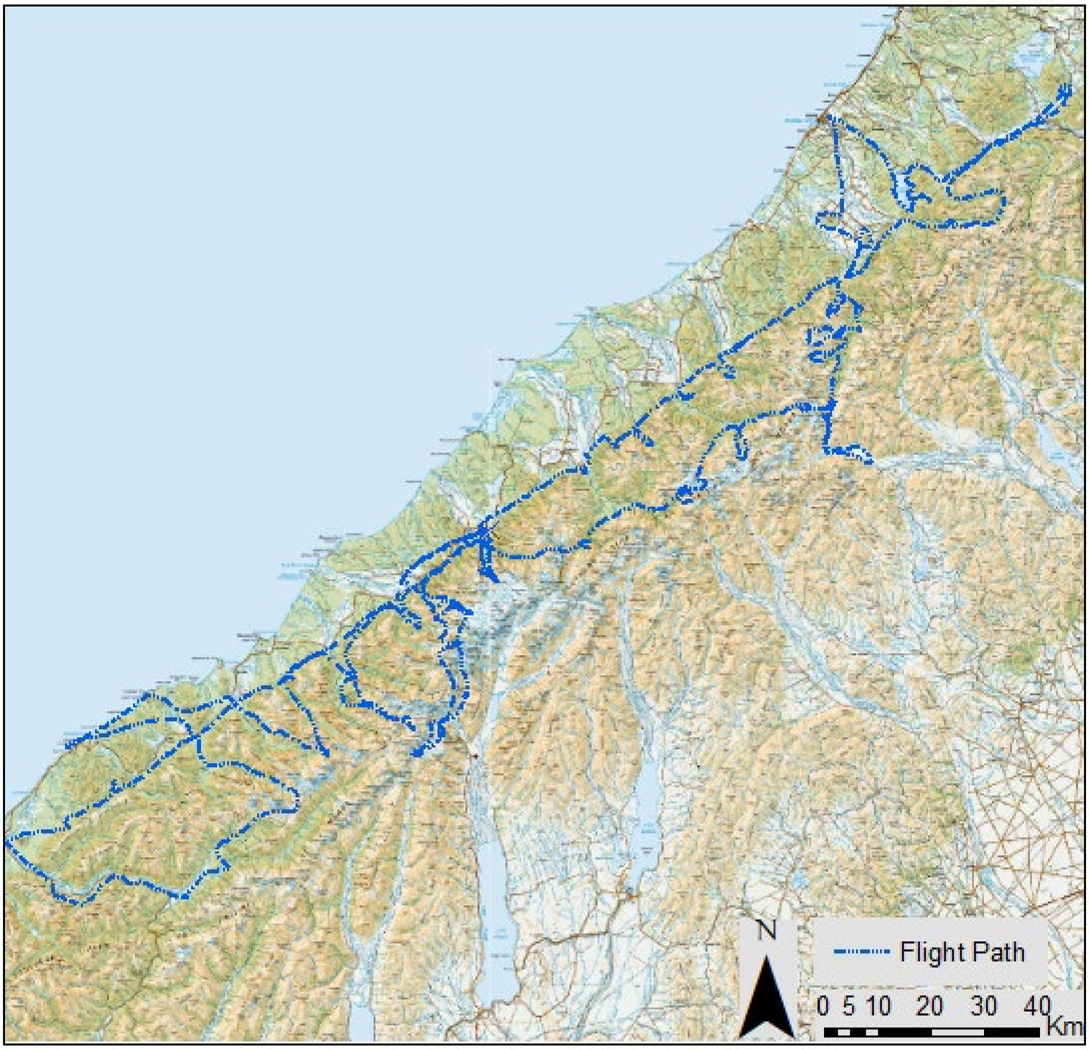

Figure 1.2 Aerial reconnaissance flight conducted on 17 and 18 April 2019 by GNS Science staff.

1.4 Landslide Distributions and Types

The technical definitions of the landslide types used in this report are taken from Hungr et al. (2014):

- A *debris avalanche* is a very rapid to extremely rapid (5 to ~10 m/s, 15–30 km/hr) shallow slide or flow of partially or fully water-saturated debris on a steep slope, which is not confined within an established channel.
- A *debris flow* is a very rapid to extremely rapid (5–10 m/s, 15–30 km/hr) flow of water-saturated, non-plastic (granular) debris in a channel. Speeds are often faster than a fit human can run. The sediment has a consistency of wet concrete, with sediment concentrations often in excess of 60% by volume (80% by weight) compared to flood waters, where sediment concentrations are generally <4% by volume (10% by weight).

During the 2019 West Coast storm event, channelised shallow debris flows were sourced in soil regolith and/or colluvium overlying weathered bedrock and were mainly initiated in heads of gullies (Figure 1.3). Some of the debris flows were strongly coupled with stream channels, which confined debris flow runout along the channel networks, while others formed fresh debris deposits on existing colluvial and alluvial fans (Figure 1.4).

Open slope debris avalanches were sourced from either bedrock or soil regolith and/or colluvium overlying weathered bedrock (Figures 1.5, 1.6 and 1.7). The open-slope debris avalanches were predominantly not coupled with stream channels. However, numerous riverbank collapses, in the form of debris avalanches, occurred along streams and river channels (Figure 1.8).

Figure 1.3 Channelised debris flow and debris fan located to the east of Lake Kaniere (Dougal Townsend, GNS Science).

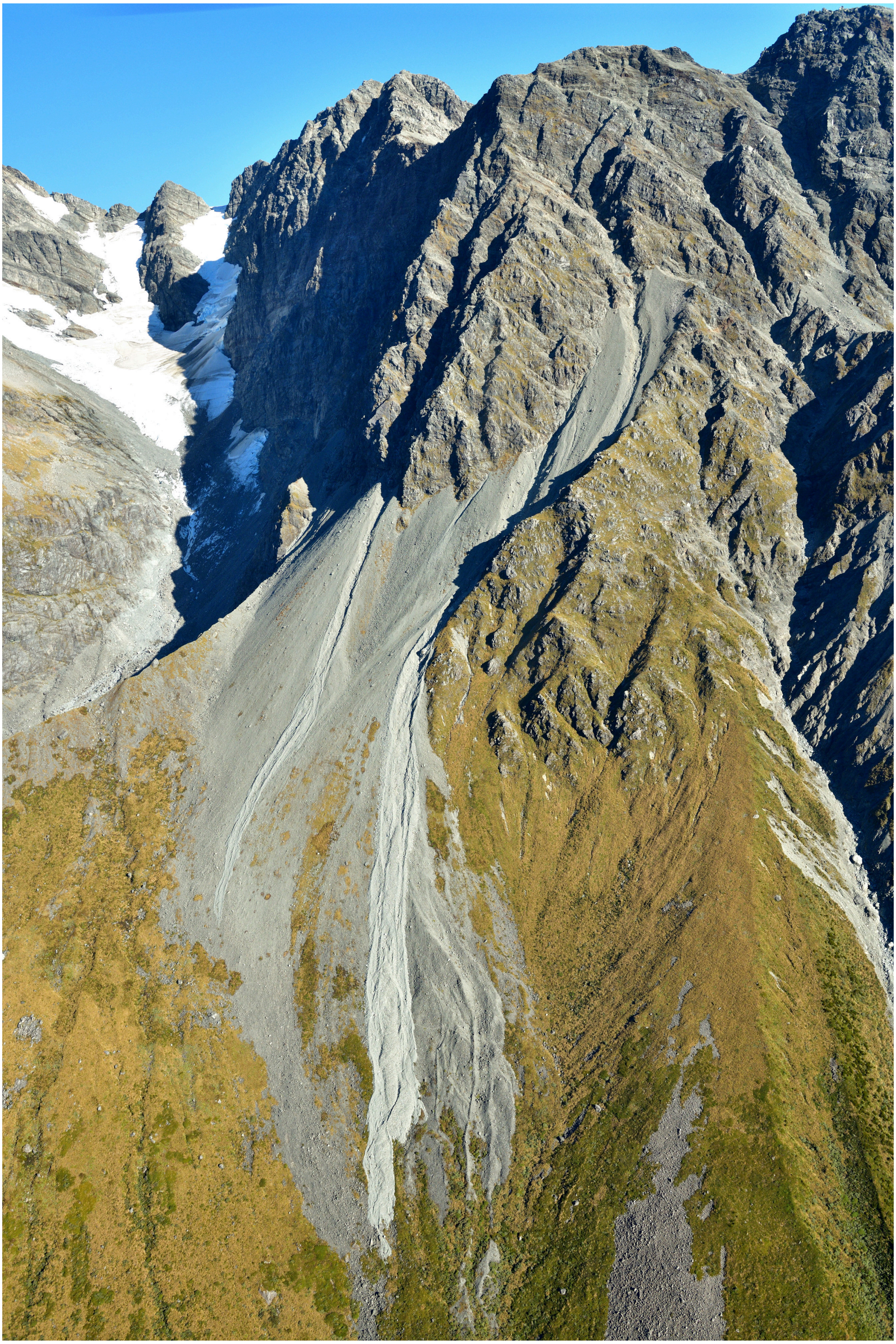

Figure 1.4 Channelised debris flow, which transitioned to an unconfined debris flow observed in the Whitcombe Valley area (Dougal Townsend, GNS Science). Note the older debris deposits on the fan, which probably occurred during similar storm events.

Figure 1.5 Open-slope debris avalanche in soil regolith observed at Kokiraki / The Doughboy, south of Lake Kaniere (Dougal Townsend, GNS Science).

Figure 1.6 Open-slope debris avalanche, comprising soil regolith and colluvial material, in the Lake Kaniere area (Dougal Townsend, GNS Science).

Figure 1.7 Open-slope debris avalanche located above a relict debris avalanche source area, comprising weathered bedrock, northeast of Haast (Dougal Townsend, GNS Science).

Figure 1.8 Riverbank erosion caused collapses in the form of localised debris avalanches, Waiho River, Franz Josef (Dougal Townsend, GNS Science).

2.0 LANDSLIDE SEVERITY ASSESSMENT METHODOLOGY

2.1 Data Sources

Satellite imagery was acquired for a c. 10,000 km² area of the West Coast, covering a section of the Southern Alps from Island Hill southwest to Mount Whitcombe (Figure 2.1). This area represented both the highest intensity of rainfall (Figure 1.1) and highest density of landslides observed from the aerial reconnaissance flight (Figure 1.2). SkySat data was acquired in a series of passes from 29 March through to 22 June, 2019. The satellite imagery has a ground resolution of 0.8 m. Google Earth historical satellite imagery and the 2016/17 Land Information New Zealand (LINZ) aerial photography (with a 0.3 m resolution) were used as pre-event imagery. These two sets of pre-event imagery were used to complement each other to achieve a full spatial coverage of the study area, with Google Earth imagery being used in areas where the pre-event LINZ imagery was insufficient.

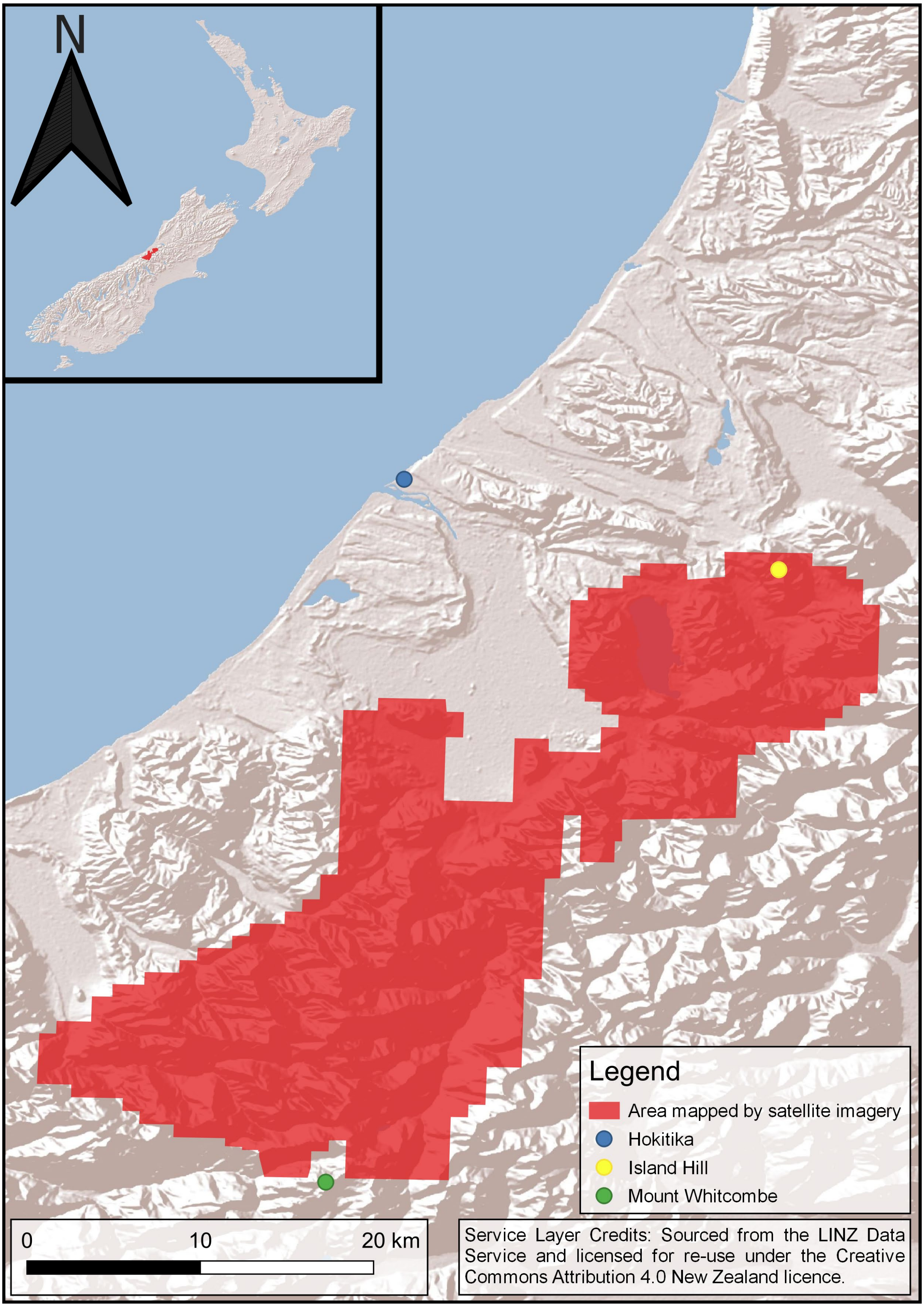

Figure 2.1 Map of the study area.

2.2 Landslide Mapping

The post-event imagery was assessed in ArcMap to identify and locate landslides. Once a landslide was identified in the post-event imagery, it was compared with the Google Earth and LINZ aerial imagery to determine whether it: (1) was newly formed, (2) had retrogressed, (3) was re-activated or (4) was a relict landslide (see the example in Figure 2.2). To ensure that all landslides within the study area were identified and mapped, we used a square grid pattern to check the full study area. The landslides were mapped manually using the same method and attributes as the Kaikōura landslide inventory (Massey et al. 2019). Each mapped landslide consisted of:

- a polygon drawn around the source area of the landslide
- a polygon drawn around the deposit area of the landslide
- inventory information unique to each landslide source and deposit filled out, and
- a point centred on the source area of the landslide.

Due to a combination of the terrain and the resolution of the imagery, it was difficult in many cases to accurately determine the type of slope failure (debris flow, rock avalanche, etc). In the case of re-activated landslides, it was difficult to determine how much of the landslide had re-activated or if it had retrogressed; because of this, the retrogressed landslides were included in the re-activated category for the analysis. Additionally, relict landslides, i.e. those that had existed prior to the March 2019 storm and had not visibly changed after the event, were mapped with a polygon around the landslide and stored as a separate feature class not used for analysis.

Each mapped landslide was also given a confidence ranking based on its area:

- Rank 0 for a landslide with an area less than 20 m^2.
- Rank 1 for a landslide with an area between 20 m^2 and 50 m^2.
- Rank 2 for a landslide with an area between 50 m^2 and 100 m^2.
- Rank 3 for a landslide with an area greater than 100 m^2.

Rank 0 landslides (a total of 70) were not included in the analysis, as they were deemed too small for accurate visual analysis and could not confidently be identified as a landslide feature and may have been some other feature, such as tree fall.

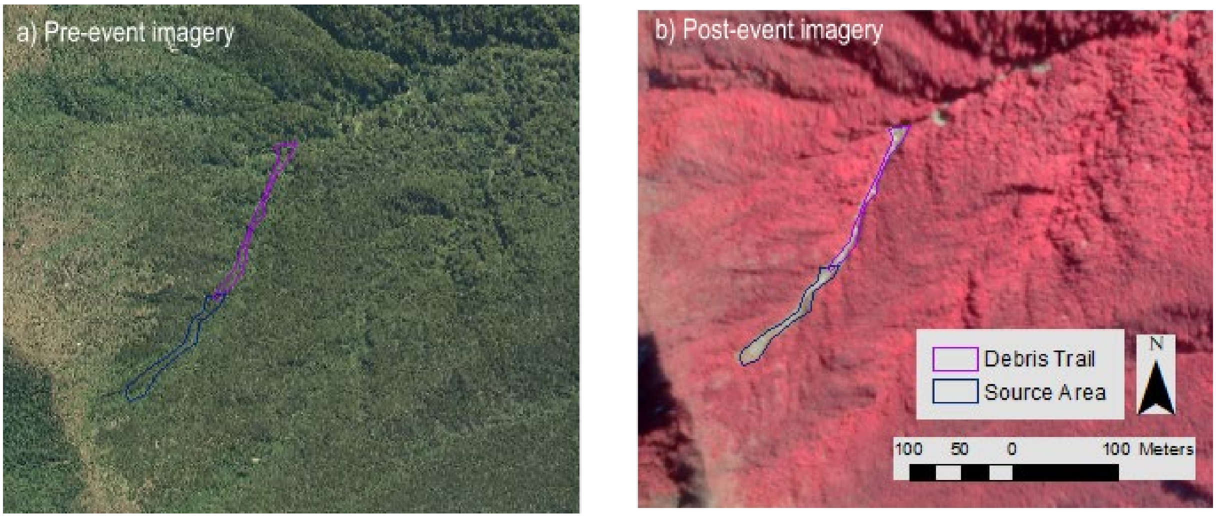

Figure 2.2 Example mapped landslide displaying the absence of the landslide in the pre-event imagery (a) and presence in post-event imagery (b), where the colour band has been adjusted.

2.3 Landslide Inventory Assessment Approach

The landslide polygons that were manually mapped from assessment of satellite images were overlaid with attribute layers containing key characteristics in ArcGIS to assess the potential influence of those characteristics in controlling the observed landslide distribution. The key characteristics included land cover, geological unit, altitude, slope angle, slope aspect and rainfall intensity. Within ArcGIS, the layers were intersected separately with the landslide source area polygons and landslide source points to extract the information unique to each landslide source. The layers used comprised:

- **Rainfall:** The 48-hour interpolated rainfall raster was reclassified into 100 mm contour intervals (isohyets) from 0 to 1300 mm, and the area covered by each interval was calculated. A landslide density (landslides/km²) was calculated for each rainfall interval.
- **Geology**: The 1:250,000-scale regional geological map (Heron 2018) was used to determine the underlying geological materials of each landslide source area. The study area contains 15 rock types (see Figure 2.4). Schist is the most abundant, underlying 40% of the study area, followed by gravel (24%) and semi-schist (15%). The remaining 12 rock types individually comprise a small percentage of the rock types in the study area. Metamorphic and sedimentary rock types that comprised less than 1% of the study area were grouped into two categories: (1) 'other metamorphic rock types', which consisted of hornfels and serpentine; and (2) 'other sedimentary rock types', which consisted of breccia, conglomerate, limestone and mudstone.
- **Land cover:** Land-cover information was obtained from the Land Cover Database v4.1 (Manaaki Whenua Landcare Research), which contained polygons for each land-cover category at 1:50,000 scale for all of New Zealand. The land-cover map (see Figure 3.3) contains 19 land-cover types, with indigenous forest covering 51% of the study area, followed by sub-alpine shrub (17%) and tussock (10%). Each of the other 16 land-cover types individually comprise a small percentage of the study area.
- **Altitude:** Elevation data was obtained from the LINZ 8-m-resolution New Zealand Digital Elevation Model (DEM). The DEM raster was re-classified into 100 m intervals from 0 to 1700 m.
- **Slope Angle:** The 8-m-resolution DEM from LINZ was used to develop a series of slope angle classes based on 10° intervals from 0° to 90°.

- **Slope Aspect**: The 8-m-resolution DEM from LINZ was used to calculate the mean slope aspect for each landslide source area. Slope aspect was re-classified into individual layers for north, northeast, east, southeast, south, southwest, west and northwest directions.

Source areas for first-time failures and re-activated landslides were separated into different layers to understand the distribution of landslides that had been generated by the March 2019 storm and those that had already existed but had become re-activated by the storm.

The total area of each feature type was calculated to determine the percentage of the study area that individual features occupied. These area calculations were used with the locations of each landslide to calculate the density of the landslides per square kilometre and the frequency ratio of landslides. The frequency ratio was calculated as:

$$Frequency\ Ratio\ = \frac{(N\ Landslides\ in\ band\ /\ Area\ of\ band)}{(Total\ N\ Landslides\ /\ Total\ study\ area)}$$

This normalised the landslide density for the total area. Landslide density and frequency ratios were calculated separately for first-time failures and re-activated landslides and the combined landslide activity within features, both for the polygon intersections and the point intersections.

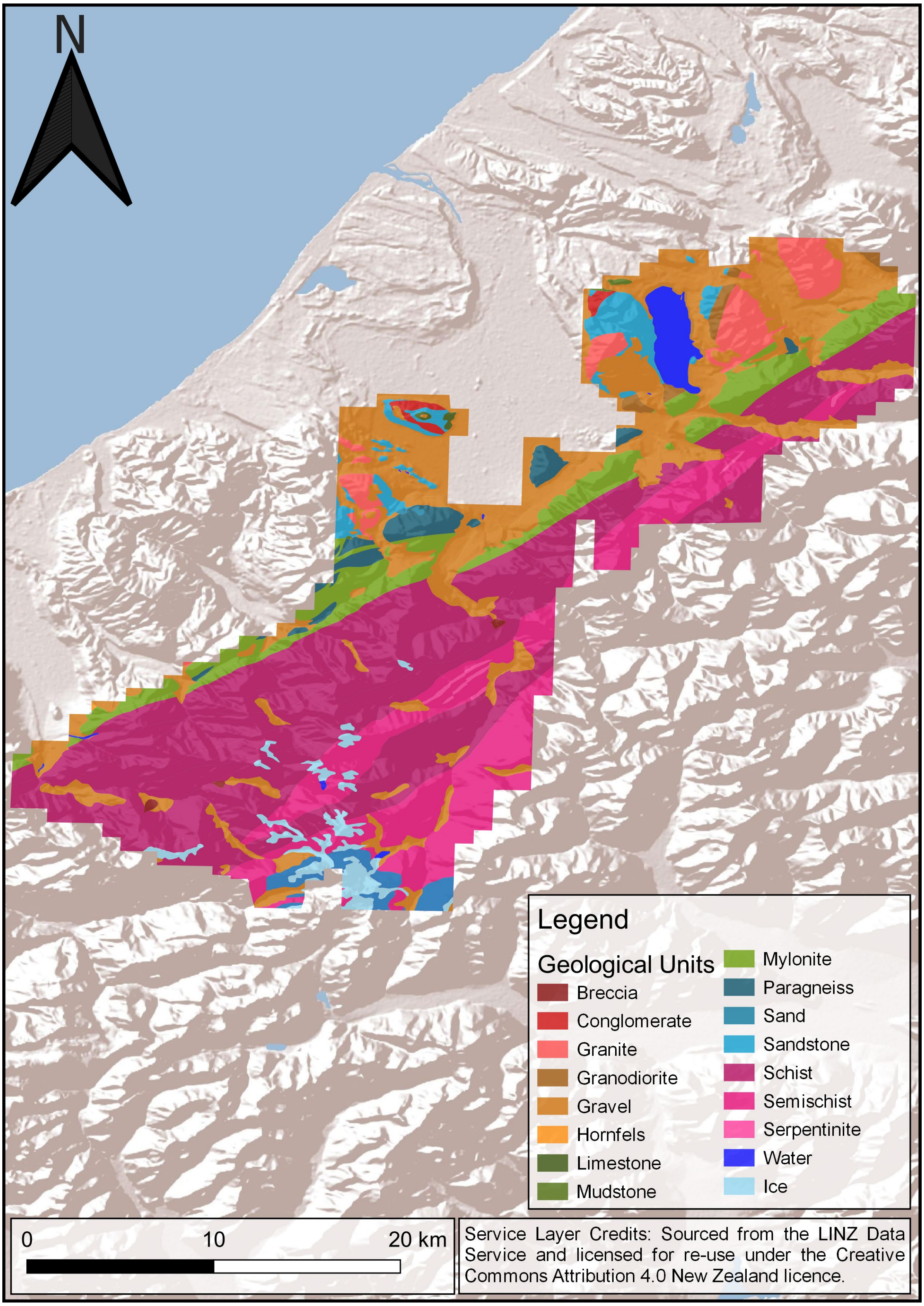

Figure 2.3 Intersection of the study area (SkySat coverage) with the main rock types from Heron (2018).

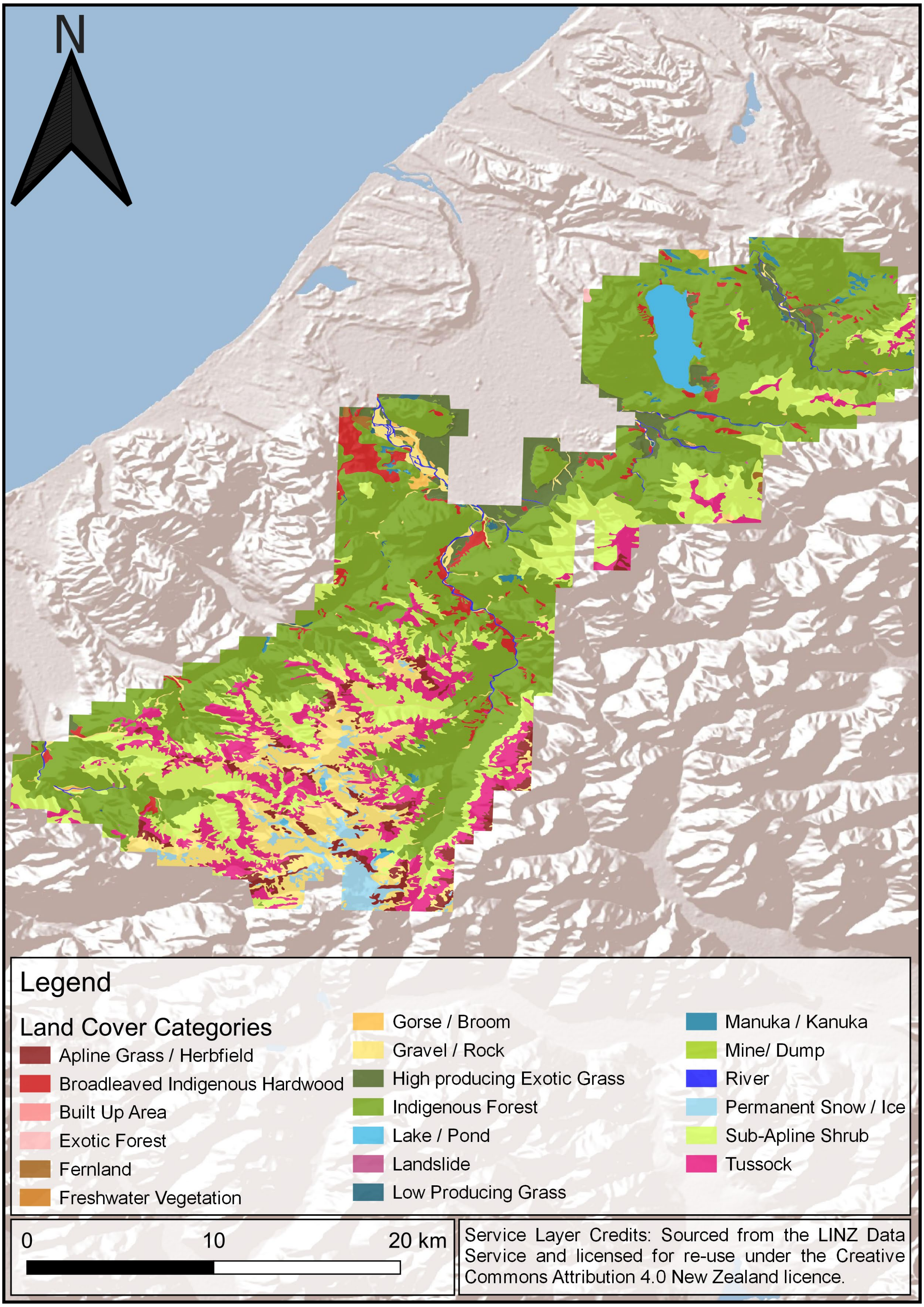

Figure 2.4 Land-cover categories from the Land Cover Database v4.1 for the study area (SkySat coverage).

3.0 LANDSLIDE SEVERITY ASSESSMENT RESULTS

Our analysis identified 1289 landslides across the study area that were triggered or re-activated during the March 2019 storm. The highest densities observed were in the hill country surrounding Mount O'Connor to the southeast of Hokitika. We identified 440 first-time failures and 849 re-activated or retrogressed landslides. The mean landslide area was 1506 m^2 and the largest was 54,805 m^2.

3.1 Landslide Density and Rainfall

The rainfall contour intervals in Figure 3.1 show that the study area received between 300 and 1300 mm of rain over the 48-hour storm period. Landslide density for each rainfall interval is shown in Figure 3.2, subdivided into first-time and retrogressed failures. The highest total landslide density of 2.56 landslides per km^2, with a frequency ratio of 1.74 (Table 3.1), was within the 500–600 mm rainfall interval. The second highest total landslide density was 2.05 landslides per km^2 with a frequency ratio of 1.39 and was within the 700–800 mm rainfall interval. The highest total number of landslides (282) was found within the 400–500 mm interval, and the highest number of first-time failures (122) was found in the 700–800 mm interval, while the highest number of re-activated landslides (202) was within the 600–700 mm interval.

Figure 3.2 shows that, within the 500–600 mm rainfall interval, the increase in landslide density is correlated with re-activated landslides, with a density of 1.96 landslides per km^2 and a frequency ratio of 2.02 (Table 3.1). The 700–800 mm rainfall interval displays the second-highest landslide density, which is correlated with an increase in the density of first-time failures at 0.94 landslides per km^2 with a frequency ratio of 0.94 (Table 3.1). The landslide density decreases for rainfall bands above 800 mm, and no landslides were mapped in areas that received between 1000 and 1300 mm of rainfall (Table 3.1).

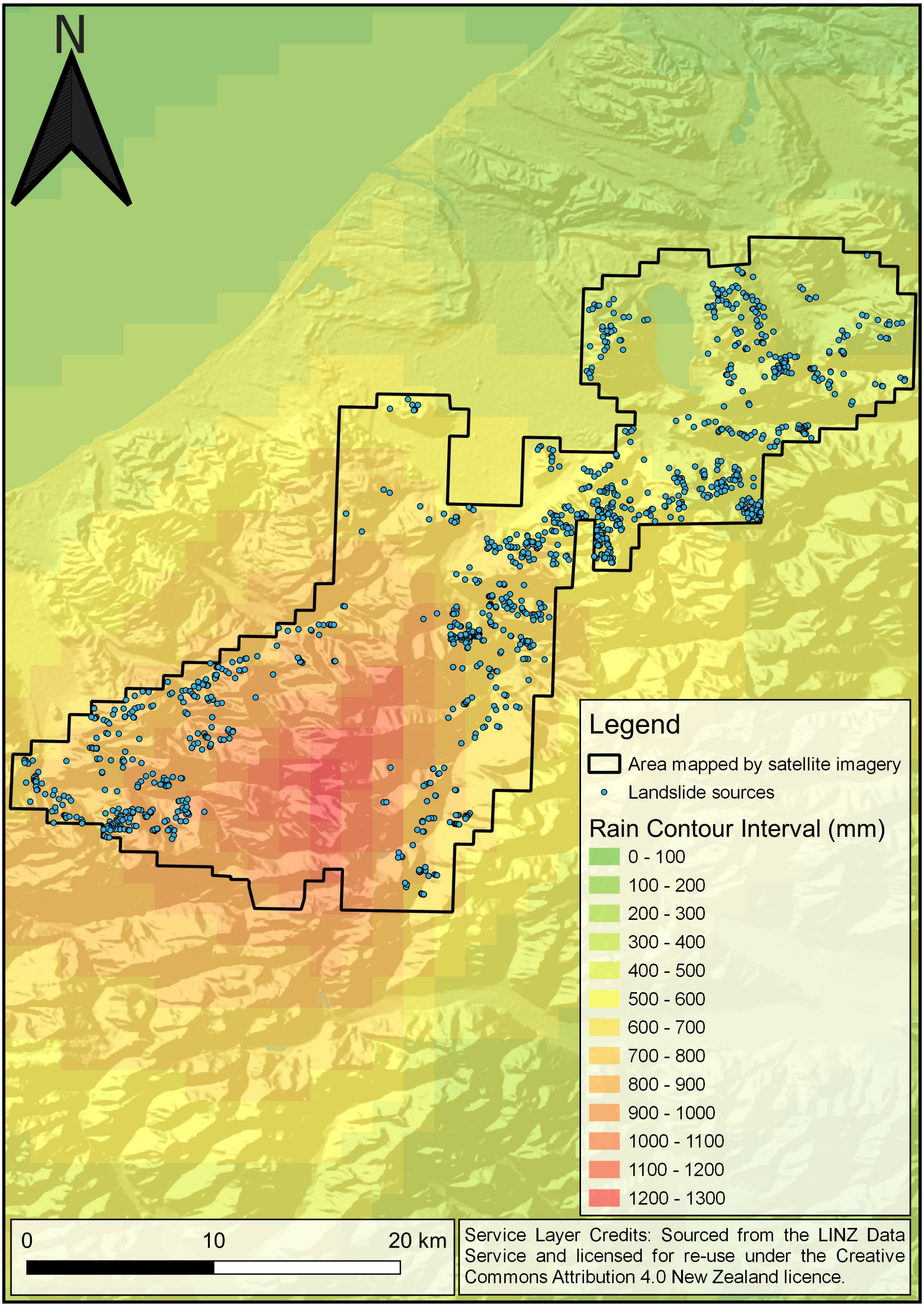

Figure 3.1 The 48-hour maximum rainfall as compared with landslide sources (both first-time failures and re-activated).

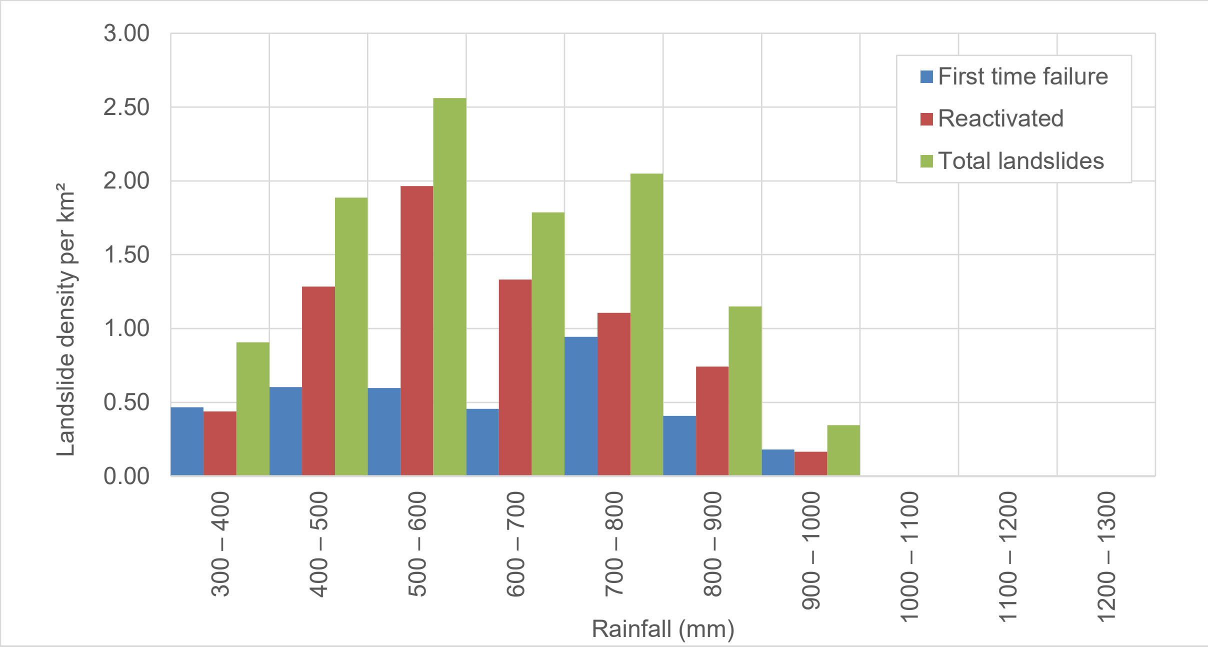

Figure 3.2 Landslide densities for both first-time failures and re-activated landslides for the different bands of 48-hour maximum rainfall.

Table 3.1 Landslide density and frequency ratio for each rainfall band.

Rainfall (mm)	Area (km^2)	% of Total Area	First-Time Failure Count	First-Time Landslide Density (per km^2)	First-Time Failure Frequency Ratio	Re-Activated Count	Re-Activated Landslide Density (per km^2)	Re-Activated Frequency Ratio	Total Activity Count	Total Landslide Density (per km^2)	Total Landslide Frequency Ratio
300–400	100.47	11.49%	47	0.47	0.93	44	0.44	0.45	91	0.91	0.61
400–500	149.42	17.09%	90	0.60	1.20	192	1.28	1.32	282	1.89	1.28
500–600	85.55	9.78%	51	0.60	1.18	168	1.96	2.02	219	2.56	1.74
600–700	151.56	17.33%	69	0.46	0.90	202	1.33	1.37	271	1.79	1.21
700–800	129.32	14.79%	122	0.94	1.87	143	1.11	1.14	265	2.05	1.39
800–900	119.94	13.72%	49	0.41	0.81	89	0.74	0.76	138	1.15	0.78
900–1000	66.58	7.61%	12	0.18	0.36	11	0.17	0.17	23	0.35	0.23
1000–1100	44.82	5.12%	0	0.00	0.00	0.00%	0.00	0.00	0	0.00	0.00
1100–1200	19.16	2.19%	0	0.00	0.00	0.00%	0.00	0.00	0	0.00	0.00
1200–1300	7.66	0.88%	0	0.00	0.00	0.00%	0.00	0.00	0	0.00	0.00

3.2 Controlling Factors for Landslide Initiation

3.2.1 Geology

Figure 3.3 displays the landslide density that occurred within each geological unit. The highest number of landslides was found within the schist category (Figure 3.2), which occupies ~40% of the study area and contained 675 landslides (223 first-time failure, 452 re-activated). Semischist had 16% of the total landslides mapped (52 first-time failure, 169 re-activated) and mylonite had 13% of the total landslide distribution (60 first-time failure, 180 re-activated).

Schist has a total landslide density of 1.85 landslides per km², semischist has a total landslide density of 1.65 landslides per km² and mylonite has a total landslide density of 2.17 landslides per km²; the categories of other metamorphic rock types (hornfels and serpentinites), granite and mylonite have the highest frequency ratios of 1.91, 1.56 and 1.47, respectively.

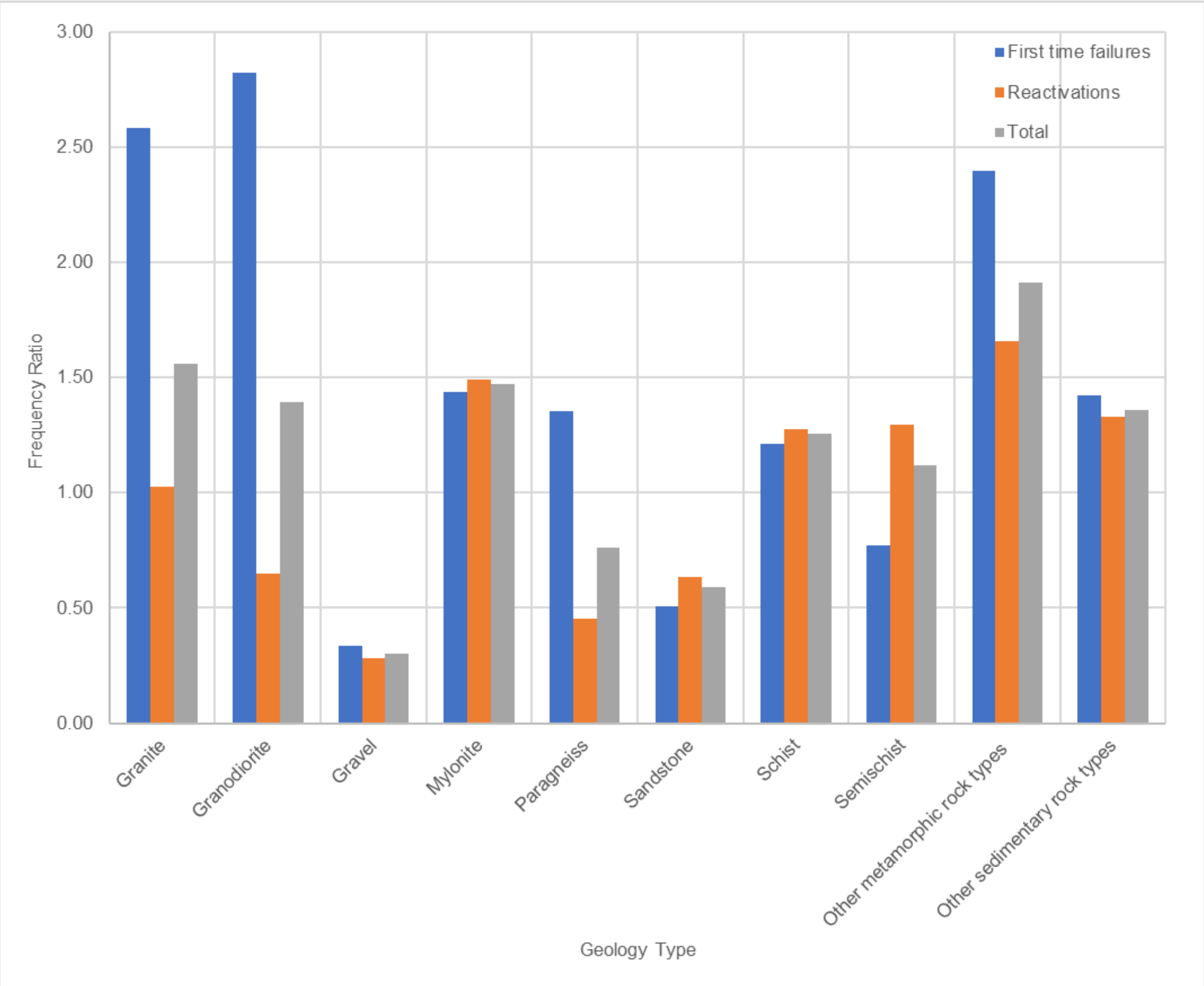

Figure 3.3 The frequency ratio for both first-time failures and re-activated landslides that occurred within each geological unit.

Table 3.2 Landslide density and frequency ratio per geology type. FtF = First-time failure.

Geology Type	Area (km^2)	% of Total Area	FtF Count	% of FtF	FtF Density (per km^2)	Frequency Ratio – FtF	Re-Activated Count	Re-Activated Density (per km^2)	% of Re-Activations	Frequency Ratio – Re-Activated	Total Activity Count	Total Landslide Density (per km^2)	% of Total Landslide Count	Frequency Ratio – Total
Granite	36.11	3.96%	47	10.22%	**1.30**	**2.58**	36	**1.00**	4.06%	**1.03**	83	**2.30**	6.16%	**1.56**
Granodiorite	6.32	0.69%	9	1.96%	**1.42**	**2.82**	4	**0.63**	0.45%	**0.65**	13	**2.06**	0.97%	**1.39**
Gravel	219.01	24.01%	37	8.04%	**0.17**	**0.34**	60	**0.27**	6.76%	**0.28**	97	**0.44**	7.20%	**0.30**
Mylonite	82.92	9.09%	60	13.04%	**0.72**	**1.44**	120	**1.45**	13.53%	**1.49**	180	**2.17**	13.36%	**1.47**
Paragneiss	20.48	2.24%	14	3.04%	**0.68**	**1.36**	9	**0.44**	1.01%	**0.45**	23	**1.12**	1.71%	**0.76**
Sandstone	39.01	4.28%	10	2.17%	**0.26**	**0.51**	24	**0.62**	2.71%	**0.63**	34	**0.87**	2.52%	**0.59**
Schist	364.55	39.96%	223	48.48%	**0.61**	**1.21**	452	**1.24**	50.96%	**1.28**	675	**1.85**	50.11%	**1.25**
Semischist	134.01	14.69%	52	11.30%	**0.39**	**0.77**	169	**1.26**	19.05%	**1.30**	221	**1.65**	16.41%	**1.12**
Other metamorphic rock types (hornfels and serpentinite)	2.48	0.27%	3	0.65%	**1.21**	**2.40**	4.00	**1.61**	0.45%	**1.66**	7.00	**2.82**	0.52%	**1.91**
Other sedimentary rock types (breccia, conglomerate, limestone and mudstone)	6.97	0.76%	5	1.09%	**0.72**	**1.42**	9.00	**1.29**	1.01%	**1.33**	14.00	**2.01**	1.04%	**1.36**

3.2.2 Land Cover

Figure 3.4 displays the frequency ratio of landslides that occurred within each land-cover type. The highest percentage of landslide activity was in the indigenous forest category (57% of total landslides), which had a total landslide count of 774 (292 first-time failures and 482 re-activated). The indigenous forest category comprises 51% of the study area. The sub-alpine shrub category had the second-highest percentage of landslides (34% of total landslides), with 461 landslides (138 first-time failures and 323 re-activated). The sub-alpine shrub category occupies 17% of the study area. The highest landslide density was observed for the 'landslide' category, with a density of 14.10 per km² and a frequency ratio of 9.86. However, the 'landslide' category has a total area of <1 km^2 and contained a total of 11 re-activated landslides (Table 3.3). The landslide category does not represent a land-cover and vegetation type. The second-highest landslide density was for sub-alpine shrub with a density of 2.96 per km² and a frequency ratio of 2.07 (Table 3.3). Broadleaf indigenous forest had the third-highest landslide density of 2.25 per km² and frequency ratio of 1.57, while indigenous forests have a landslide density of 1.6 per km² and frequency ratio of 1.12.

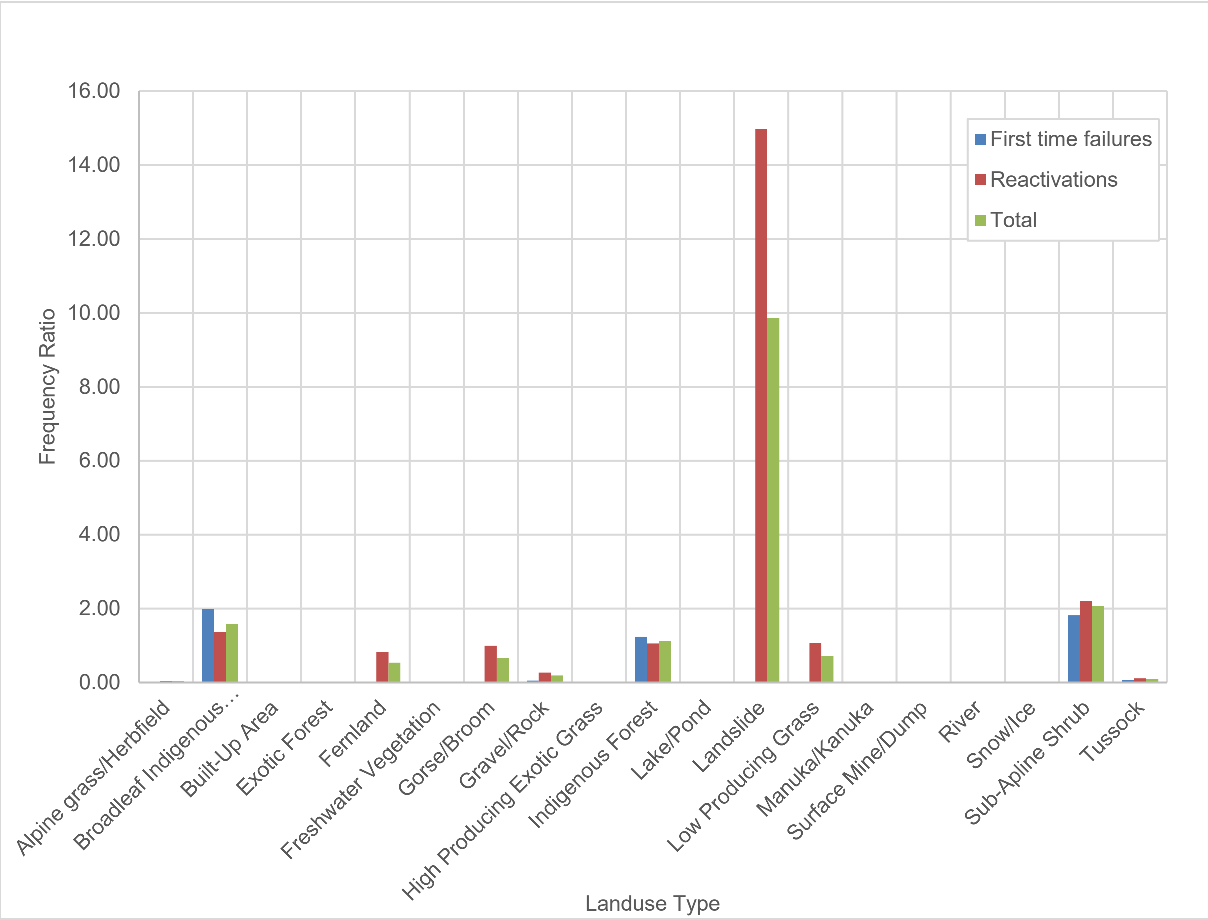

Figure 3.4 The frequency ratio of landslides for both first-time failures and re-activated landslides that occurred within each land-cover type.

Table 3.3 Landslide density and frequency ratio per land-cover type.

Land-Cover Type	Area (km^2)	% of Total Area	First-Time Landslide Count	First-Time Landslide Density (per km²)	First-Time Landslide Frequency Ratio	Re-Activated Landslide Count	Re-Activated Landslide Density (per km²)	Re-Activated Landslide Frequency Ratio	Total Landslide Count	Total Landslide Density (per km²)	Total Landslide Frequency Ratio
Alpine Grass / Herbfield	22.73	2.41%	0	0.00	0.00	1	0.04	0.05	1	0.04	0.03
Broadleaf Indigenous Hardwood	25.78	2.74%	25	0.97	1.99	33	1.28	1.36	58	2.25	1.57
Built-Up Area	0.07	0.01%	0	0.00	0.00	0	0.00	0.00	0	0.00	0.00
Exotic Forest	0.39	0.04%	0	0.00	0.00	0	0.00	0.00	0	0.00	0.00
Fernland	1.29	0.14%	0	0.00	0.00	1	0.77	0.82	1	0.77	0.54
Freshwater Vegetation	0.02	0.00%	0	0.00	0.00	0	0.00	0.00	0	0.00	0.00
Gorse/Broom	3.20	0.34%	0	0.00	0.00	3	0.94	1.00	3	0.94	0.66
Gravel/Rock	79.75	8.46%	2	0.03	0.05	20	0.25	0.27	22	0.28	0.19
High-Producing Exotic Grass	31.61	3.35%	0	0.00	0.00	0	0.00	0.00	0	0.00	0.00
Indigenous Forest	483.26	51.28%	292	0.60	1.24	482	1.00	1.06	774	1.60	1.12
Lake/Pond	11.12	1.18%	0	0.00	0.00	0	0.00	0.00	0	0.00	0.00
Landslide	0.78	0.08%	0	0.00	0.00	11	14.10	14.98	11	14.10	9.86
Low-Producing Grass	2.96	0.31%	0	0.00	0.00	3	1.01	1.08	3	1.01	0.71
Manuka/Kanuka	5.56	0.59%	0	0.00	0.00	0	0.00	0.00	0	0.00	0.00
Surface Mine / Dump	0.02	0.00%	0	0.00	0.00	0	0.00	0.00	0	0.00	0.00
River	5.29	0.56%	0	0.00	0.00	0	0.00	0.00	0	0.00	0.00
Snow/Ice	17.46	1.85%	0	0.00	0.00	0	0.00	0.00	0	0.00	0.00
Sub-Alpine Shrub	155.53	16.50%	138	0.89	1.82	323	2.08	2.21	461	2.96	2.07
Tussock	95.55	10.14%	3	0.03	0.06	10	0.10	0.11	13	0.14	0.10

3.2.3 Altitude

Elevation in the study area ranges from <100 to 1700 m above mean sea level. Figure 3.5 displays the landslide frequency ratio for different altitude bands. The highest total landslide density is observed at altitudes between 900 and 1200 m. The total landslide density is highest at 1000–1100 m with 3.06 landslides per km^2 and a frequency ratio of 2.01, followed by 2.56 landslides per km² and a frequency ratio of 1.68 at altitudes of 900–1000 m and a density of 2.42 landslides/km² and frequency ratio of 1.59 for 1100–1200 m (see Table 3.4). Low numbers of landslides were observed for altitudes greater than 1200 m.

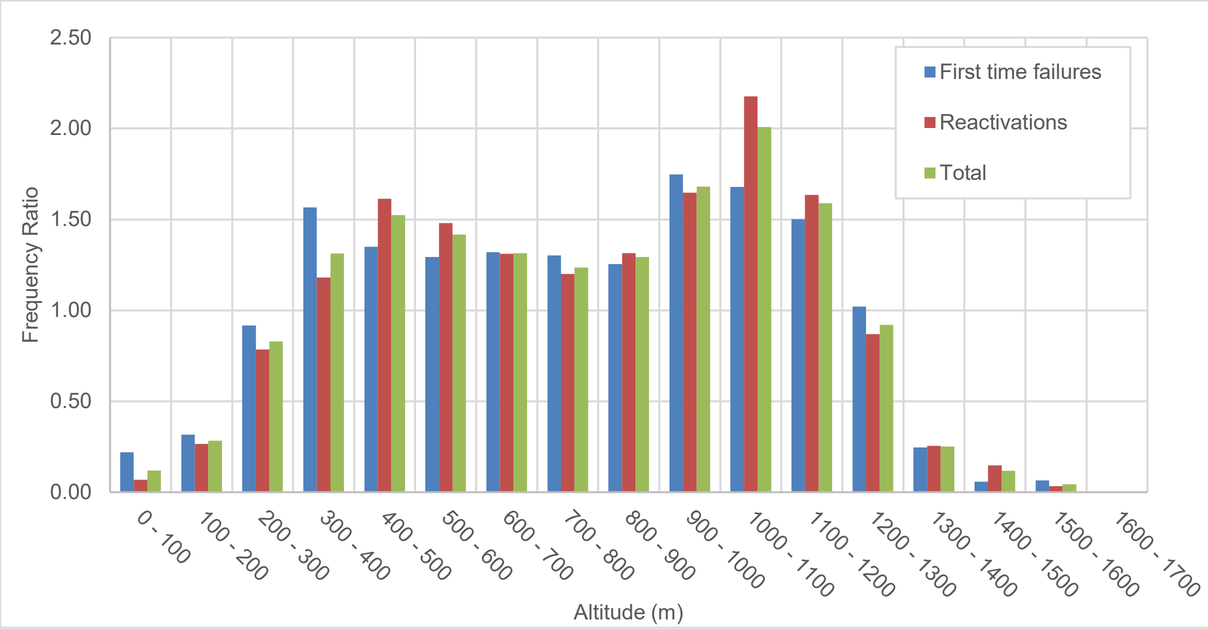

Figure 3.5 Frequency ratios for both first-time failures and re-activated landslides for the different altitude levels.

Table 3.4 Landslide density and frequency ratio per altitude band.

Altitude (m)	Area (km^2)	% of Total Area	First-Time Landslide Count	First-Time Landslide Density (per km²)	First-Time Landslide Frequency Ratio	Re-Activated Landslide Count	Re-Activated Landslide Density (per km²)	Re-Activated Frequency Ratio	Total Landslide Count	Total Landslide Density (per km²)	Total Landslide Frequency Ratio
0–100	43.76	4.90%	5	0.11	**0.22**	3	0.07	**0.07**	8	0.18	**0.12**
100–200	97.51	10.91%	16	0.16	**0.32**	26	0.27	**0.27**	42	0.43	**0.28**
200–300	80.03	8.96%	38	0.47	**0.92**	63	0.79	**0.78**	101	1.26	**0.83**
300–400	64.09	7.17%	52	0.81	**1.57**	76	1.19	**1.18**	128	2.00	**1.31**
400–500	62.96	7.05%	44	0.70	**1.35**	102	1.62	**1.61**	146	2.32	**1.52**
500–600	62.64	7.01%	42	0.67	**1.29**	93	1.48	**1.48**	135	2.16	**1.42**
600–700	58.51	6.55%	40	0.68	**1.32**	77	1.32	**1.31**	117	2.00	**1.31**
700–800	54.81	6.13%	37	0.68	**1.30**	66	1.20	**1.20**	103	1.88	**1.23**
800–900	52.29	5.85%	34	0.65	**1.25**	69	1.32	**1.31**	103	1.97	**1.29**
900–1000	50.82	5.69%	46	0.91	**1.75**	84	1.65	**1.65**	130	2.56	**1.68**
1000–1100	49.43	5.53%	43	0.87	**1.68**	108	2.19	**2.18**	151	3.06	**2.01**
1100–1200	46.3	5.18%	36	0.78	**1.50**	76	1.64	**1.64**	112	2.42	**1.59**
1200–1300	43.52	4.87%	23	0.53	**1.02**	38	0.87	**0.87**	61	1.40	**0.92**
1300–1400	39.1	4.38%	5	0.13	**0.25**	10	0.26	**0.25**	15	0.38	**0.25**
1400–1500	33.71	3.77%	1	0.03	**0.06**	5	0.15	**0.15**	6	0.18	**0.12**
1500–1600	29.94	3.35%	1	0.03	**0.06**	1	0.03	**0.03**	2	0.07	**0.04**
1600–1700	24.17	2.70%	0	0.00	**0.00**	0	0.00	**0.00**	0	0.00	**0.00**

3.2.4 Slope Angle

Figure 3.6 displays the landslide frequency ratio for different slope angle categories, with landslide frequency increasing for steeper slopes up to 70°. The highest total landslide density of 4.59 landslides/km^2 and a frequency ratio of 3.32 was observed for slope angles between 60° and 70°. Beyond 70°, the landslide frequency decreases, with no landslides observed in the 80° to 90° slope interval (Table 3.5).

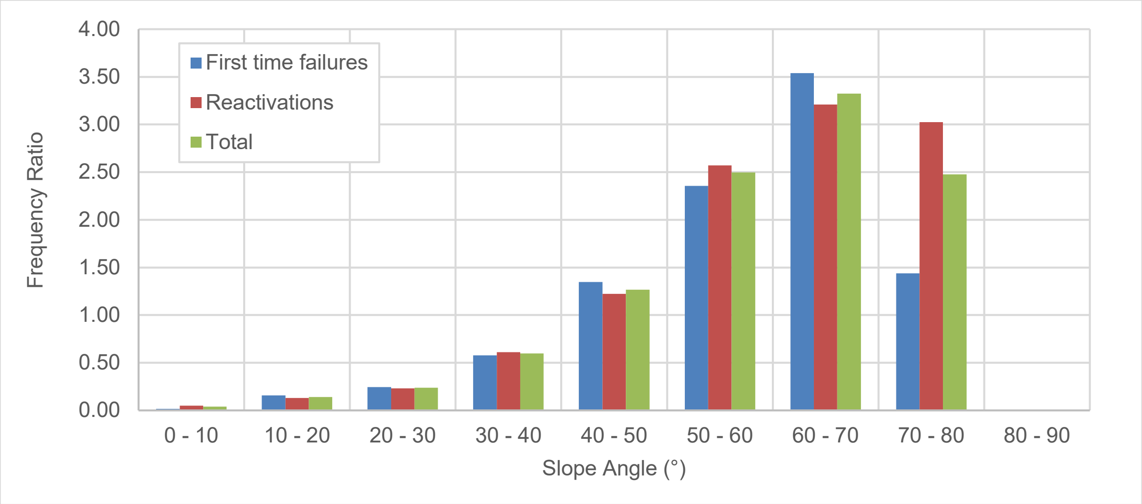

Figure 3.6 Frequency ratios for both first-time failures and re-activated landslides for the different slope angles.

Table 3.5 Landslide density and frequency ratio per slope angle band.

Slope Angle	Area (km^2)	% of Total Area	First-Time Landslide Count	First-Time Landslide Density (per km^2)	First-Time Landslide Frequency Ratio	Re-Activated Landslide Count	Re-Activated Landslide Density (per km^2)	Re-Activated Landslide Frequency Ratio	Total Landslide Count	Total Landslide Density (per km^2)	Total Landslide Frequency Ratio
0–10°	128.71	12.52%	1	0.01	0.02	6	0.05	0.05	7	0.05	0.04
10–20°	93.57	9.10%	7	0.07	0.16	11	0.12	0.13	18	0.19	0.14
20–30°	128.14	12.46%	15	0.12	0.25	27	0.21	0.23	42	0.33	0.24
30–40°	211.53	20.57%	58	0.27	0.58	117	0.55	0.61	175	0.83	0.60
40–50°	272.90	26.54%	175	0.64	1.35	302	1.11	1.22	477	1.75	1.27
50–60°	161.64	15.72%	181	1.12	2.35	376	2.33	2.57	557	3.45	2.50
60–70°	30.30	2.95%	51	1.68	3.54	88	2.90	3.21	139	4.59	3.32
70–80°	1.46	0.14%	1	0.68	1.44	4	2.74	3.02	5	3.42	2.48
80–90°	0.01	0.00%	0	0.00	0.00	0	0.00	0.00	0	0.00	0.00

3.2.5 Slope Aspect

Figure 3.7 displays landslide frequency ratios for different slopes aspects. Slopes that face north, northeast, and northwest have the highest landslide densities of 3.21, 2.29 and 2.31 landslides per km^2, respectively. Together, these slopes make up 43.2% of the total study area and contain 77.5% of landslides mapped.

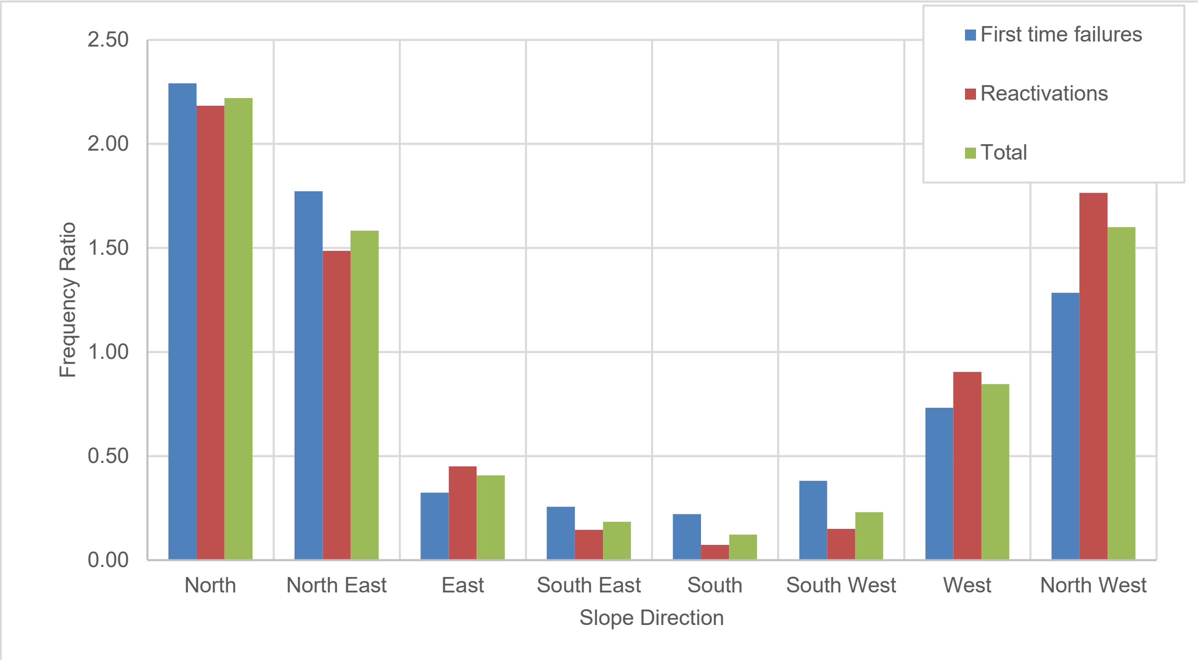

Figure 3.7 Frequency ratios for both first-time failures and re-activated landslides that occurred within each slope aspect band.

Table 3.6 Landslide density and frequency ratio per slope aspect category.

Aspect	Area (km^2)	% of Total Area	First-Time Landslide Count	First-Time Landslide Density (per km^2)	First-Time Landslide Frequency Ratio	Re-Activated Landslide Count	Re-Activated Landslide Density (per km^2)	Re-Activated Landslide Frequency Ratio	Total Landslide Count	Total Landslide Density (per km^2)	Total Landslide Frequency Ratio
North (337.5–22.5°)	136.23	14.61%	154	1.13	2.29	283	2.08	2.18	437	3.21	2.22
Northeast (22.5–67.5°)	128.03	13.73%	112	0.87	1.77	181	1.41	1.49	293	2.29	1.58
East (67.5–112.5°)	100.17	10.74%	16	0.16	0.32	43	0.43	0.45	59	0.59	0.41
Southeast (112.5–157.5°)	86.67	9.30%	11	0.13	0.26	12	0.14	0.15	23	0.27	0.18
South (157.5–202.5°)	100.96	10.83%	11	0.11	0.22	7	0.07	0.07	18	0.18	0.12
Southwest (202.5–247.5°)	111.42	11.95%	21	0.19	0.38	16	0.14	0.15	37	0.33	0.23
West (247.5–292.5°)	130.04	13.95%	47	0.36	0.73	112	0.86	0.91	159	1.22	0.85
Northwest (292.5–337.5°)	138.80	14.89%	88	0.63	1.28	233	1.68	1.76	321	2.31	1.60

4.0 DISCUSSION

The landslide inventory includes no observed landslide activity in areas with rainfall greater than 1000 mm for this storm. The highest density of landslide activity (Figure 3.2) was within the 500–600 mm rainfall interval, consisting almost entirely of re-activated landslides, with the second-highest landslide density recorded for the 700–800 mm rainfall interval, where the density of newly generated landslides is almost equal to that of re-activated landslides. However, for a high-intensity rainfall event, it may be expected that the highest density of landslides would correlate with areas of highest rainfall. Precipitation tends to increase in relation to altitude in a process known as orographic enhancement (Napoli et al. 2019). Therefore, if the rainfall intensity was increasing with altitude, then an increase in landslide density at high altitude (and high rainfall) may be expected. However, the landslide density observed for the March 2019 storm does not increase with altitude. Instead, our data displays the highest landslide density (Figure 3.4) for altitudes between 1000 and 1100 m. The absence of landslides mapped at both high rainfall and high altitude may be a result of several factors, including:

1. The limitations of mapping from satellite imagery.
    a. Landslides may have occurred but cannot routinely be detected using optical imagery on the scree slopes that are typical of high altitudes within the region.
    b. Slopes facing in a south/southeast direction were obscured by shadow, so landslides here may not have been detected.
    c. Higher-altitude areas were covered with snow at either the time that the pre-event imagery was captured or at the time that the post-event satellite imagery was taken, which may have obscured any landslides that occurred in these locations.
2. The limitations of the rain gauge data.
    a. The rain gauge data may not accurately represent the distribution of rainfall over the study area, with interpolation ‘smoothing’ out rainfall across the South Island as a whole. Importantly, there is only one rain gauge within the study area, so variations in rainfall across the study area would not be captured in this data.
    b. The linear interpolation between the rain gauges. This method of smoothing the discrete data may be an incorrect assumption, as the rainfall would likely vary depending on topography. For example, when the storm front reaches the range front of the mountains, orographic overturning may result in higher rainfall on the lower slopes (Houze and Medina 2003).
    c. Rain gauge measurements do not capture variations in rainfall intensity during the 48-hour storm period, and this missing variation in rainfall may have influenced the landslide distribution.

A possible solution to the limitations of satellite imagery may be to use change detection from 3D surface models captured immediately pre- and post-storm. The inclusion of rain radar data may help alleviate some of the limitations of the rain gauge data by providing both a higher spatial and temporal resolution of rainfall during the storm event. Including rain radar data may also help investigate whether different rainfall thresholds for new landslide initiation and landslide re-activation exist, as suggested by the differences in landslide type and density for the 500–600 mm rainfall interval and 700–800 mm rainfall interval. Confirming these rainfall thresholds could provide more accurate landslide hazard forecasting for future storm events in the region and elsewhere. Other factors, such as slope angle and aspect, may also influence the distribution of landslides. Landslide density was observed to increase with slope angle, up to about 70° (Figure 3.5). However, slopes greater than 70° account for less than 0.2% of the study area, and landslides on such slopes were likely to be obscured by shadow or difficult to identify if they were exposed rock prior to the storm.

Additionally, the indigenous forest land-cover category covers more than half of the study area. It has a lower landslide frequency than the sub-alpine shrub category, which comprises of 17% of the study area. This increased density in the sub-alpine shrub category may be related to the altitude, with a landslide frequency peak from 900–1200 m, as the treeline in the South Island can be as low as 900 m (Heenan and McGlone 2013). Vegetation type can have an impact on the stability of slopes, with forests having a greater stabilising effect on the cohesion of slopes than grasses and shrubs (Kokutse et al. 2016), and the forest canopies can intercept rain drops before they reach the ground and reduce the impact on soil erosion (Keim and Skaugset 2003). These factors may together explain the increase in landslide density in the sub-alpine zone.

Landslides also preferentially occurred on north-, northwest- and northeast-facing slopes. The relationship between slope aspect and landslide density may be influenced by the direction that the storm travelled as it made landfall on the west coast. Further analysis of rain radar data on the direction and travel of the storm will help us to understand the relationship between slope aspect, rainfall and landslide density. Due to orographic effects, which increase rainfall on the windward side of slopes, it is expected that the higher density of landslides would be on slopes facing in directions closest to the storm as it moved inland. However, due to the shadow on the satellite imagery of south/southeast-facing slopes, landslides that did occur on leeward slopes may not have been identified.

The physiographic attributes of slope aspect, slope angle, land-cover type, altitude and rock type are all attributes that pre-dispose a particular slope to landsliding. Landslide susceptibility maps, which determine where landslides are likely to occur, correlate the occurrence of landslide with pre-disposing factors (Reichenbach et al. 2018). However, due to the limitations of our landslide inventory in the inability to detect landslides in steep, alpine, snow-covered terrain, caution is required when correlating the physiographic attributes with the landslide inventory to determine landslide susceptibility.

5.0 CONCLUSIONS

The 2019 West Coast storm occurred during the week of 25–31 March 2019, in which the storm broke national records for rainfall measurements over a 48-hour period, leading to a state of emergency being declared for the West Coast region. Significant damage to infrastructure and roading occurred due to floodwaters and landsliding. An aerial reconnaissance was flown by GNS Science on 17 and 18 April 2019 to identify landslides triggered by the storm as part of a GeoNet landslide response. High-resolution SkySat satellite imagery was subsequently captured for a 10,000 km² area, which extended from inland of Hokitika south to Harihari. This satellite imagery, combined with pre-storm-event aerial imagery obtained from LINZ and Google Earth, was used to map the distribution of landslides that were triggered by the March 2019 storm. The storm event triggered 1289 landslides within the mapped study area, with the highest densities observed in the hill country surrounding Mount O'Connor to the southeast of Hokitika. The landslide distribution was overlaid onto attribute layers containing key physiographic characteristics (rainfall, geology, slope angle, slope aspect, vegetation type) to assess the correlation between these slope characteristics and the occurrence of landslides.

The results of our analysis have shown that the more intense rainfall did not appear to result in a greater density of landslide activity. This pattern of distribution could be the result of the interpolated rainfall data not being representative of the true rainfall during the event and may indicate that the rainfall on the slopes closer to the coast was higher than indicated by the linear interpolation of the rain gauge data. Additionally, the limitations of the satellite imagery, which include snow cover and shadow, may have prevented the mapping of landslides at higher altitudes. The inclusion of other rainfall data from rain radar may provide a more complete analysis of the landslides that were able to be mapped for this study area. This could provide more accurate landslide hazard predictions for future storm events in the region.

While the density distributions across the study area do not correlate with rainfall intensity, they do correlate with slope angle, where landslide density increases with steeper slopes and slope aspect. North-, northwest-, and northeast-facing slopes all display a higher landslide density, which may be related to the characteristics of the rainfall in the storm event. For the major land-cover types, sub-alpine shrub displays the highest landslide frequency ratio of 2.07 and accounts for 16.5% of the study area. The dominant land-cover type of indigenous forest, accounting for 51.28% of the study area, only displays a landslide frequency ratio of 1.57. This suggests that vegetation may be a control on landslide occurrence.

6.0 ACKNOWLEDGMENTS

Funding for this project was provided through GeoNet and the summer student scholarship at Victoria University of Wellington.

7.0 REFERENCES

Heenan PB, McGlone MS. 2013. Evolution of New Zealand alpine and open-habitat plant species during the late Cenozoic. *New Zealand Journal of Ecology*. 37(1):105–113.

Heron DW, custodian. 2018. Geological map of New Zealand [map]. 2nd ed. Lower Hutt (NZ): GNS Science. 1 USB, scale 1:250,000. (GNS Science geological map; 1).

Houze RA, Jr, Medina S. 2003. Orographic enhancement of precipitation in midlatitudes: results from MAP and IMPROVE II. Seattle (WA): University of Washington; [accessed 2021 Jul]. https://atmos.washington.edu/MG/PDFs/prep03_houz_orographic.pdf

Hungr O, Leroueil S, Picarelli L. 2014. The Varnes classification of landslide types, an update. *Landslides*. 11(2):167–194. doi:10.1007/s10346-013-0436-y.

Keim RF, Skaugset AE. 2003. Modelling effects of forest canopies on slope stability. *Hydrological Processes*. 17(7):1457–1467. doi:10.1002/hyp.5121.

Kokutse NK, Temgoua AGT, Kavazović Z. 2016. Slope stability and vegetation: conceptual and numerical investigation of mechanical effects. *Ecological Engineering*. 86:146–153. doi:10.1016/j.ecoleng.2015.11.005.

Massey CI, Townsend DB, Dellow GD, Lukovic B, Rosser BJ, Archibald GC, Villeneuve M, Davidson J, Jones KE, Morgenstern R, et al. 2019. Kaikoura Earthquake Short-Term Project: landslide inventory and landslide dam assessments. Lower Hutt (NZ): GNS Science. 43 p. (GNS Science report; 2018/19).

MetService. 2008–2021. Wellington (NZ): MetService. Warnings & watches; [accessed 2021 Jul 28]. https://www.metservice.com/warnings/home#weather-criteria

Napoli A, Crespi A, Ragone F, Maugeri M, Pasquero C. 2019. Variability of orographic enhancement of precipitation in the Alpine region. *Scientific Reports*. 9:13352. doi:10.1038/s41598-019-49974-5.

NIWA Weather. 2019 Mar 27. Auckland (NZ): NIWA Forecasting Services. NIWA can confirm that Cropp waterfall observed 1086 mm in 48 hours, the highest 48 hour rainfall total for New Zealand on record [Tweet]; [accessed 2021 Jul]. https://twitter.com/NiwaWeather/status/1110688913448828928

Reichenbach P, Rossi M, Malamud BD, Mihir M, Guzzetti F. 2018. A review of statistically-based landslide susceptibility models. *Earth-Science Reviews*. 180:60–91. doi:10.1016/j.earscirev.2018.03.001.

www.gns.cri.nz

Principal Location

1 Fairway Drive, Avalon
Lower Hutt 5010
PO Box 30368
Lower Hutt 5040
New Zealand
T +64-4-570 1444
F +64-4-570 4600

Other Locations

Dunedin Research Centre
764 Cumberland Street
Private Bag 1930
Dunedin 9054
New Zealand
T +64-3-477 4050
F +64-3-477 5232

Wairakei Research Centre
114 Karetoto Road
Private Bag 2000
Taupo 3352
New Zealand
T +64-7-374 8211
F +64-7-374 8199

National Isotope Centre
30 Gracefield Road
PO Box 30368
Lower Hutt 5040
New Zealand
T +64-4-570 1444
F +64-4-570 4657